*J. Fluid Mech.* (1991), *vol.* 231, *pp.* 665–688
*Printed in Great Britain*

# Optical studies on the turbulent motion of solid particles in a pipe flow

By JAMES B. YOUNG AND THOMAS J. HANRATTY
Department of Chemical Engineering, University of Illinois, Urbana, IL 61801, USA

(Received 15 January 1990 and in revised for 15 April 1991)

An extension of an axial viewing optical technique (first used by Lee, Adrian & Hanratty) is described which allows the determination of the turbulence characteristics of solid particles being transported by water in a pipe. Measurements are presented of the mean radial velocity, the mean rate of change radial velocity, the mean-square of the radial and circumferential fluctuations, the Eulerian turbulent diffusion coefficient, and the Lagrangian turbulent diffusion coefficient. A particular focus is to explore the influence of slip velocity for particles which have small time constants. It is found that with increasing slip velocity the magnitude of the turbulent velocity fluctuations remains unchanged but that the turbulent diffusivity decreases. The measurements of the average rate of change of particle velocity are consistent with the notion that particles move from regions of high fluid turbulence to regions of low fluid turbulence. Measurements of the root-mean-square of the fluctuations of the rate of change of particle velocity allow an estimation of the average magnitude of the particle slip in a highly turbulent flow, which needs to be known to analyse the motion of particles not experiencing a Stokes drag.

## 1. Introduction

Small particles in a turbulent flow will assume a haphazard motion in response to the drag associated with the fluctuating fluid velocity. If the particle has a different density to the fluid, it will not follow the fluid motion. The analysis of turbulent fluid–particle systems is impeded because of the lack of data on the relation between the turbulence characteristics of particles and those of the fluid.

This paper describes an extension of the optical technique that was recently used by Lee, Hanratty & Adrian (1989) to study the motion of droplets in a gas that is flowing turbulently through a pipe. The technique has two novel aspects: (i) The use of axial viewing photography filters out the much larger axial flow component so that accurate measurements of turbulent motion in planes perpendicular to the flow are possible. (ii) Direct (rather than the usual indirect) measurements are made of local mass fluxes needed to define Eulerian eddy diffusion coefficients.

Results are presented in this paper on the motion of solid spheres in water flowing down a vertical 5.08 cm pipe. Glass or steel spheres, with diameters of 100 μm, were injected from a 0.5 mm tube in the centre of the pipe at nearly the same velocity as the water.

In one set of experiments the cross-section of the pipe was illuminated along a 3–5 mm length by flash units that were located on both sides of the pipe. The positions of the particles were photographed by a camera located at the bottom of the pipe, which views axially upward. If enough photographs are taken, a statistically significant number of particle images can be analysed to obtain a concentration profile, $\bar{C}(r)$. By repeating this experiment at different distances from the injector, $z$, the dispersion of the particles, $\overline{X_{\mathrm{P}}^2}$, versus time, $t$, can be determined. Here, $\overline{X_{\mathrm{P}}^2}$ is the mean-squared $x$-displacement of the particles from the centre of the distribution and $t = z/\bar{V}_z$, where $V_z$ is the mean particle velocity in the flow direction. The Lagrangian turbulent diffusivity is determined from the relation $\epsilon_{\mathrm{LP}} = \frac{1}{2}(\mathrm{d}\overline{X_{\mathrm{P}}^2}/\mathrm{d}t)$ for large $t$.

In a second set of experiments, the velocity components of the particles in a plane perpendicular to the mean flow are determined by using five coloured flashes located immediately downstream of one another. The time intervals between the flashes were adjusted so as to obtain at least three images of a particle as it moved down the pipe. Particle velocities were calculated from the measured distances between the images and the known time intervals. The velocities at a given $r$ are designated by $V_i = \bar{V}_i + v_i$, where $\bar{V}_i$ is the average for a large number of particles and $v_i$ is the deviation from the average. Similarly, the rate of change of velocity is designated as $A_i = \bar{A}_i + a_i$, where $A_i = \mathrm{d}V_i/\mathrm{d}t$. Because of symmetry $\overline{V_\theta} \approx 0$. The radial flux is

$$N(r) = \overline{V_{\mathrm{R}}}(r)\,\bar{C}(r). \tag{1}$$

The Eulerian turbulent diffusivity can thus be obtained from measurements of $\overline{V_{\mathrm{R}}}$ and the concentration profile since

$$\epsilon_{\mathrm{EP}} = N(r) \bigg/ \left(-\frac{\mathrm{d}\bar{C}}{\mathrm{d}r}\right). \tag{2}$$

The use of a colour-coded flash arrangement to determine the direction of particle motion proved to be a significant improvement over the method, used by Lee *et al.*, of defocusing one of the images. In particular, it could determine small displacements for which the images of the particles overlapped.

In the experiments of Lee *et al.*, the droplets had large time constants. They lagged the air flow so that the turbulence characteristics of the particles were quite different from those of the fluid. The experiments reported in this paper for 100 μm glass spheres in water were performed under conditions for which the particles followed the fluid; i.e. they had a small time constant. This provided an opportunity to examine the accuracy of the method by comparing measured particle turbulence with known fluid turbulence. The experiments with stainless steel spheres were done to examine the behaviour of particles with small time constants and large free-fall velocities. These results are of interest in that they provide a check on theoretical predictions (Reeks 1977; Pismen & Nir 1978; Nir & Pismen 1979) that the particles should have the same fluctuating velocity as the fluid, but a much smaller turbulent diffusivity.

Although the main focus of the experiments was the determination of particle turbulence in the central regions of the pipe where the fluid turbulence is approximately homogeneous, some interesting results on the effect of the non-homogeneity of the turbulence were obtained. The time-average of $\mathrm{d}V_\theta/\mathrm{d}t$ is zero. However, the time-average of $\mathrm{d}V_{\mathrm{R}}/\mathrm{d}t$ was found to be non-zero, and to be related to the spatial change in $\overline{v_{\mathrm{R}}^2}$. This is consistent with the notion of turbophoresis whereby particles tend to move from regions of high fluid turbulence to regions of low fluid turbulence.

Most theoretical analyses of particle motion in a turbulent field assume that fluid drag is described by Stokes law. A major limitation in extending such analyses to situations where this law is not valid is the determination of the average slip velocity in a highly turbulent flow. This paper shows how this quantity can be estimated from measurements of the root-mean-square of the fluctuations in the rate of change of particle velocity.

## 2. Theory

### 2.1. *Lagrangian analysis*

The Lagrangian analysis of the dispersion of particles from a point source in a homogeneous field is described by Taylor's (1921) relation

$$\frac{1}{2}\frac{\mathrm{d}\overline{X_{\mathrm{P}}^2}}{\mathrm{d}t}=\int_0^t \overline{v(0)\,v(s)}\,\mathrm{d}s, \tag{3}$$

where $X_{\mathrm{P}}$ is the $x$-displacement of a particle from the source position at time, $t$, and $\overline{X_{\mathrm{P}}^2}$ is an average for a large number of particles. The correlation, $\overline{v(0)\,v(s)}$, is an average of the product of the particle velocity at times zero and $s$. If the turbulence characteristics of the particles have reached a stationary state then the mean-square value of the turbulent velocity fluctuations of the particles at time zero, $\overline{v^2(0)}$, may be considered to be a statistical property of the particle turbulence, defined as $\overline{v^2}$. Therefore it is convenient to write (3) as

$$\frac{1}{2}\frac{\mathrm{d}\overline{X_{\mathrm{P}}^2}}{\mathrm{d}t}=\overline{v^2}\int_0^t \frac{\overline{v(0)\,v(s)}}{\overline{v^2}}\,\mathrm{d}s. \tag{4}$$

The correlation coefficient in (4) varies from 1 at $s=0$ to 0 at $s=\infty$. A Lagrangian timescale can be defined as

$$T_{\mathrm{LP}}=\int_0^\infty \frac{\overline{v(0)\,v(s)}}{\overline{v^2}}\,\mathrm{d}s, \tag{5}$$

so that the turbulent diffusion coefficient and the Lagrangian lengthscale are

$$\epsilon_{\mathrm{LP}}=\overline{v^2}\,T_{\mathrm{LP}}, \tag{6}$$

$$L=(\overline{v^2})^{\frac{1}{2}}\,T_{\mathrm{LP}}. \tag{7}$$

Considerable recent work has been done on the limitations of the application of the dispersion concept to particles and the respective advantages and disadvantages of the Eulerian and Lagrangian approaches. See, for example, a recent summary by Gouesbet, Desjonqueres & Berlemont (1988).

### 2.2. *Particle equation of motion*

Relationships of $\overline{v^2}$ and $\epsilon_{\mathrm{LP}}$ to fluid turbulence properties can be developed by solving the equation of motion of the particle. Different formulations of this equation have been used. The relation derived by Maxey & Riley (1983) now seems to be generally accepted for particle motion at low Reynolds and acceleration numbers. A simplified version of this equation, valid for large ratios of particle to fluid density, is as follows:

$$\frac{\mathrm{d}\boldsymbol{v}}{\mathrm{d}t}=\beta(\boldsymbol{u}-\boldsymbol{v}), \tag{8}$$

with

$$\beta=\frac{3C_{\mathrm{D}}\rho_{\mathrm{F}}}{4d_{\mathrm{P}}\rho_{\mathrm{P}}}|U-V|, \tag{9}$$

where $C_{\mathrm{D}}$ is the drag-coefficient, $d_{\mathrm{P}}$ is the particle diameter, $|U-V|$ is the magnitude of the difference between the particle and fluid velocities, $\boldsymbol{v}$ is the fluctuating particle velocity and $\boldsymbol{u}$ is the fluctuating fluid velocity. The quantity $1/\beta$ is a time constant which characterizes the ability of the particle to follow the fluid turbulence. The product of $1/\beta$ and the particle velocity is a measure of the stopping distance if the particle were moving in a stagnant fluid. For a spherical particle small enough that Stokes law is applicable

$$\beta = \frac{18\mu_F}{d_P^2 \rho_P}, \tag{10}$$

where $\mu_F$ is the fluid viscosity.

Even though the density ratio $\rho_P/\rho_F$ is not exceptionally large in the experiments described in this paper, a simplified equation of the same form as (8) can be used with

$$\tilde{\beta} = \frac{3C_D \rho_F |U - V|}{2d_P(2\rho_P + \rho_F)} \tag{11}$$

in the place of $\beta$. For low particle Reynolds numbers,

$$\tilde{\beta} = \frac{36\mu_F}{(2\rho_P + \rho_F)d_P^2}. \tag{12}$$

This result can be obtained by using the Fourier analysis of the full equation of particle motion to estimate the order of magnitude of the different terms (Hinze 1975; Young 1989).

Equation (8) can be solved to relate statistical properties of $\boldsymbol{v}$ to statistical properties of $\boldsymbol{u}$. The recent analyses of Reeks, Pismen & Nir, and Nir & Pismen for Stokesian particles in a homogeneous, isotropic field are the most complete treatment of this problem. However, the results of these studies have not yet been fully tested.

The analysis of particles that do not obey Stokes law is more complicated because the term $C_D|U - V|$, in (9) or (11) is a function of the relative velocity. For a fully developed field the relative velocity is

$$V_R = \boldsymbol{i}_z(\bar{V}_Z - \bar{U}_Z) + \boldsymbol{i}_x(v_X - u_X) + \boldsymbol{i}_y(v_Y - u_X) + \boldsymbol{i}_z(v_Z - u_Z), \tag{13}$$

where $\bar{V}_Z$, $\bar{U}_Z$ are the average particle and fluid velocities, $v_i, u_i$ are the components of the fluctuating velocities, and $\boldsymbol{i}_x, \boldsymbol{i}_y, \boldsymbol{i}_z$ are unit vectors. From (13) and (11) it is seen that if Stokes law is not valid that $\tilde{\beta}$ is, in general, a function of the fluctuating velocity, so that equation (8) is no longer linear in the fluctuating velocity. One approach is to calculate some average effective relative velocity:

$$\overline{|U - V|^2} = \overline{(V - U)^2} = (\bar{V}_Z - \bar{U}_Z)^2 + \sum_{i=1}^{3} \overline{(v_i - u_i)^2}. \tag{14}$$

If it can be assumed that turbulence terms in (14) can be neglected relative to $(\bar{V}_Z - \bar{U}_Z)$ then

$$|V_R| = \bar{V}_Z - \bar{U}_Z, \tag{15}$$

where, for the experiments discussed in this paper, $(\bar{V}_Z - \bar{U}_Z)$ is the terminal velocity of the particles, $V_T$. Equation (15) is a good approximation at low fluid flow rates. However, since $V_T$ is constant and $\overline{(v_i - u_i)^2}$ increases with the flow rate, it could be a poor approximation at high flows.

### 2.3. *Forces due to flow non-homogeneity*

No rigorous treatment of particle motion in a non-homogenous turbulent flow is available. However, a number of possible effects have been identified: The close proximity of a wall can increase drag (Risk & Elghobashi 1985). Lift forces can exist because of particle rotation and mean shear. Drift velocities arise because of the response of the particles to turbulent velocity fluctuations whose statistical properties are varying in space.

Saffman (1965, 1968) showed that, in a shear flow, the lift due to particle rotation can be neglected. He developed the following relation for the lift force on a particle in a steady laminar flow due to uniform simple shear:

$$F_L = 6.46\,\mu_F\,(\tfrac{1}{2}d_P)^2\left(\frac{1}{\nu_F}\frac{dU_Z}{dy}\right)^{\frac{1}{2}}(U_Z - V_Z). \tag{16}$$

Here it should be noted that $\nu_F$ is the kinematic viscosity of the fluid. If the particle leads the fluid then $F_L$ is negative, i.e. toward the wall. If the particle lags the fluid $F_L$ is positive. The results of Saffman are restricted to low particle Reynolds numbers, relatively large shear, and small particle sizes, i.e.

$$\epsilon = \frac{\left(\frac{dU}{dy}\right)^{\frac{1}{2}}\nu_F^{\frac{1}{2}}}{|U-V|} \gg 1, \quad Re_G = \left(\frac{dU}{dy}\right)\frac{(d_P)^2}{\nu_F} \ll 1. \tag{17}$$

Equation (16) has sometimes been used to interpret measurements of time-averaged particle distributions in turbulent flow by substituting $d\bar{U}_z/dy$ and $(\bar{U}_z - \bar{V}_z)$ into (16).

The response of a particle to the fluid velocity fluctuations whose statistical properties are varying in space can give rise to a time-average drift velocity in the direction of decreasing turbulent intensity. The following equation can be derived for a Cartesian coordinate system (Reeks 1983; Caporaloni *et al.* 1975):

$$V_{Di} = -\frac{1}{\tilde{\beta}}\left(\frac{\partial\,\overline{v_i v_j}}{\partial x_j}\right). \tag{18}$$

Both Reeks and Caporaloni gave this effect the name turbophoresis and Reeks called $V_{Di}$ the turbophoretic velocity.

### 2.4. *Scaling*

From a consideration of the discussion in §2(*a–c*) three dimensionless groups can be defined which are useful in interpreting the results.

Group $\tilde{\beta}T_{LF}$ represents the ratio of the timescale of the particle motion to the timescale of the fluid. A large value of $\tilde{\beta}T_{LF}$ means that the particles will follow the fluid motion. It is expected that $\overline{v^2}/\overline{u^2}$ will be unity for large $\tilde{\beta}T_{LF}$ and will decrease with decreasing $\tilde{\beta}T_{LF}$.

Group $V_T/v^*$ represents the ratio of free fall velocity $|\bar{U}-\bar{V}|$ to the friction velocity (or to the magnitude of the turbulent fluid velocity fluctuations). For large values of $V_T/v^*$ the particle, in falling through the fluid, will encounter a fluid turbulence which is rapidly changing direction. As a consequence the Lagrangian timescale characterizing the particle motion, $T_{LP}$, will be smaller than for the case when $V_T \approx 0$. From (6) it is seen that this leads to a decrease in the particle diffusivity, $\epsilon_{LP}$. This is known as Yudine's crossing trajectories effect (Yudine 1959; Csanady 1963).

Group $\tau^+ = (1/\tilde{\beta})/(\nu_F/v^{*2})$ is the ratio of the particle time constant to the time constant characterizing the viscous wall region. When $\tau^+ > 20$–$30$, the stopping distance of the particles is greater than the thickness of the viscous wall region and non-homogeneities close to the wall are not important (McCoy & Hanratty 1977).

## 3. Description of the experiments

### 3.1. *The flow system*

A complete description of the flow system in which the experiments were performed is given in the thesis by Young (1989).

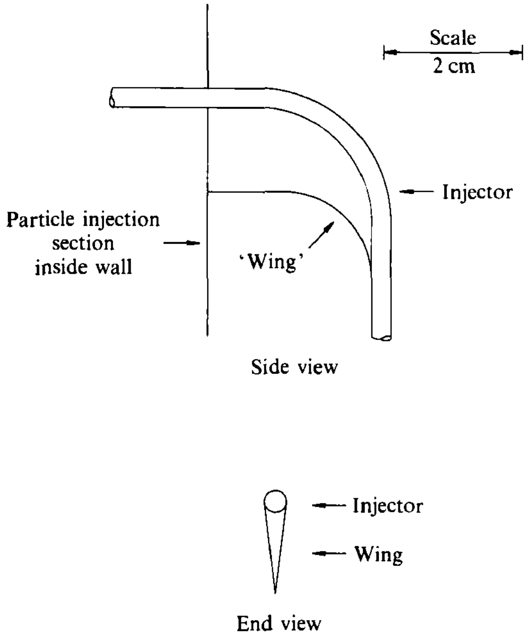

FIGURE 1. Side and end view of drag-reducing wing.

Deionized and deaerated water, whose temperature was controlled, was circulated down a 5.08 cm i.d., 6.4 m long vertical Plexiglas pipe. Measurements were always carried out at least 90 pipe diameters from the inlet to assure fully developed turbulent flow. Particles of diameter 100 μm were injected as a slurry directly into the pipe and then separated from the water after the exit of the section. The particles were always injected to give an average particle volume concentration of 1 p.p.m. in the pipe cross-section.

The particle injection system consisted of a liquid–solid fluidized bed, a bellows metering pump, a surge cup, a particle injector, and a particle injector tip. The particles were always fluidized to give a volume concentration of approximately 8200 p.p.m. in the bed. The slurry was withdrawn from the bed with a bellows metering pump (built by Gorman Rupp Industries). The surge cup, with a pressurized air space, was positioned between the bellows pump and the injector to help even out the flow rate of the slurry. The injector consisted of a 0.317 cm o.d. stainless steel tube. This tubing made a right-angle turn and exited through the sidewall of the pipe. The bend in the injector was radiused to avoid particle plugging. Since turbulence formed behind the horizontal leg of the tubing could cause asymmetries in the flow, the wing shown in figure 1 was used. The injector tip, brazed onto the end of the injector tube, was fabricated from a 3.3 cm length of 0.317 cm o.d. stainless steel rod. The i.d. of the finished tip changes, after 2.3 cm, from 0.132 cm to 0.051 cm. The outside of the tip was tapered so that the wall thickness at the outlet averages 0.0025 cm. The vertical distance from the horizontal arm to the bottom of the tip was 8.1 cm. With an 8200 p.p.m. slurry concentration and a slurry velocity through the lower part of the tip equal to the centreline velocity, the average particle volume concentration in the pipe cross-section was 1 p.p.m.

The glass particles used in the experiments were Class IV, Number 1217 Unispheres manufactured by Ferro Corporation's Cataphote Division. They have a 1.51 refractive index and a 2.42 specific gravity. The 316 stainless steel spheres, which

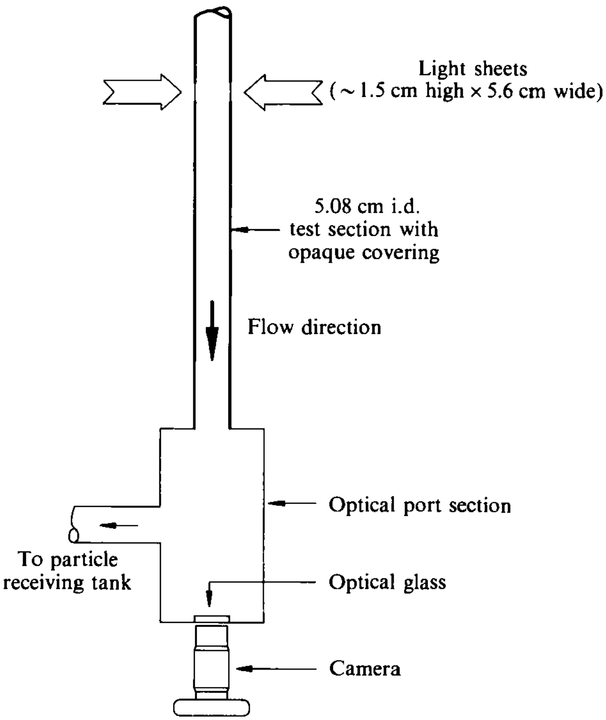

FIGURE 2. Axial viewing photographic technique.

have an 8.0 specific gravity, were obtained from Duke Scientific Corporation. Both the glass and stainless steel particles were thoroughly sieved such that only those in the 90–106 μm diameter range were used. In addition, the glass particles were rolled down an inclined plane to separate the more spherical particles from the less spherical ones (Young 1989). The stainless steel particles were quite spherical and needed no further separation.

The particle–liquid mixture exited through the optical port section sketched in figure 2. For most of the runs, the fluid velocity was large enough that the particles were swept out of this section and into a collection tank for later use. For runs with stainless steel particles at low flow velocities, some particles collected in the optical port section. This caused no problem since the number collected during the period of photographing was quite small. These could be swept out quite easily by momentarily increasing the flow rate.

### 3.2. *Photographic techniques*

The particles in the test section were photographed with a 35 mm camera (equipped with an 80–200 mm *f*4.5 macro focusing zoom lens, a motor drive, and ISO/ASA 400 speed film) placed at the bottom of the test section, as shown in figure 2. The camera was positioned to look vertically upward and was focused on a plane a certain distance away. At that plane, particles in the pipe cross-section were illuminated with xenon tube electronic units that were focused onto the pipe wall with spherical focusing lenses. The flash units and focusing lenses rested on two horizontal platforms that could be traversed vertically.

The camera and flash units were automatically triggered with a control box. One relay cord, connecting the box to the camera, opened the shutter and provided power to the camera window after the shutter closed. A second relay cord was connected to a light synchronization unit. This unit was equipped with five delay timers that could be set and used according to the type of data desired.

The quality of the particle images depended on both camera focus and aperture setting. The focus was empirically set before placing the camera on a small platform (that was located under the viewing port at the bottom of the pipe) since the pipe wall could not be properly focused upon. The aperture was set to obtain both the sharpest and brightest particle images possible and a good image of the pipe wall. An aperture which was too wide produced large particle images that had a diffuse star-shaped boundary and superb images of the pipe wall. An aperture which was too narrow produced dim images of the particles and the pipe wall. For glass particles at the optimum camera settings, the individual particle images varied widely in both size and intensity. For stainless steel particles, the images were much more uniform. From these observations, it was concluded that non-homogeneities on the surface or inside the glass spheres caused differences in individual particle intensity, not non-homogeneities in light sheet intensity.

When the positions of individual particles were desired to obtain concentration profiles, the delay timer apparatus was set to trigger two flash units simultaneously. The placement of the two flash units on opposite sides of the pipe assured that each particle image obtained on the negative was always in approximately the correct position relative to the pipe wall. This was especially important for the stainless steel particles since only half of the particle is illuminated by each flash unit. The pipe was always covered with opaque material except for the slit that was illuminated. The slit height used for these measurements was either 3, 5, or 10 mm depending on the distance from the injector tip (the greater the distance, the greater the slit height).

Multiple position measurements of individual particles were made with the scheme shown in figure 3. Five flash units were sequentially triggered, with the delay timer apparatus, to illuminate five planes covering a total distance of 5 cm. The direction of particle motion was determined by placing colour filters in front of each flash unit. The colours red, orange, yellow-green, light blue, and violet were chosen because they were sufficiently different from each other on film and because the intensities of the different images produced by the same particle were approximately the same. For colour image photography, a flash pulse duration of 330 μs was used in order to obtain images of sufficient intensity. For the studies reported in this paper, the particles travelled a very small distance during this time; consequently, image streaks were not formed. Only a 180 μs pulse duration was needed for the black and white (concentration profile) photography. The filters attached to the flash units were constructed by sandwiching dyed glycerine between two thin Plexiglas sheets. Colour reversal (slide) film was used for the multiple image photography.

All negatives and slides were manually analysed with a Mitutoyo PJ 311 profile projector. The position of each particle image in relation to the pipe wall image was located and recorded on a computer for later analysis. The image of the pipe wall on film was always between 0.6 and 1.3 cm in diameter. The profile projector was capable of measurement to within 0.0001 cm and the width of the cross-hairs on the analyser compared to the particle image diameter meant that each image could be easily centred upon. Thus, the measurement of each particle image position was repeatable to within about 0.0002 cm on each axis. The particle concentration used in the studies was low enough to be able to assume that each image was formed by a single particle. In most cases, groups of images formed from a single particle when using multiple flashes, were easily located. For situations in which both the $r$- and $\theta$-

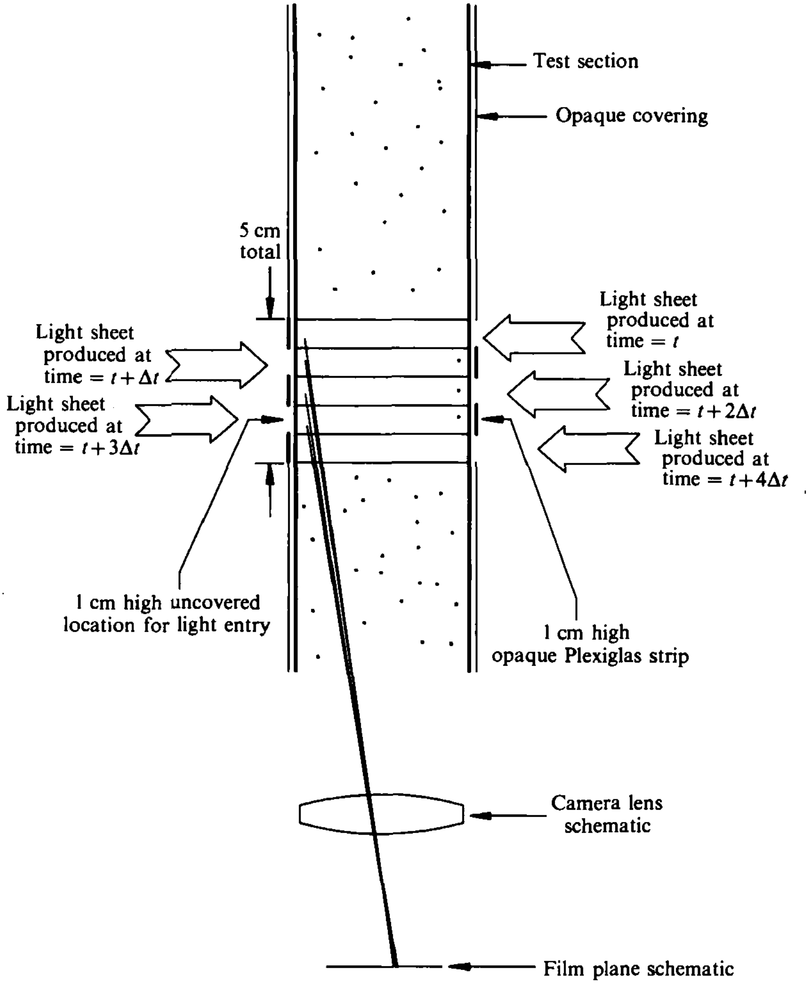

FIGURE 3. Multiple image axial viewing photographic technique.

velocities were very small, overlapping images were occasionally produced (< 2%). On colour film, they usually appeared as a larger image with the different colours around its boundary. On black and white film, overlapped images could not be distinguished. The use of five flashes in the multiple image technique meant that at least three images of each particle were usually obtained except for those, located very close to the pipe wall, that had small axial velocities.

### 3.3. *Treatment of the photographic data*

In analysing the multiple image data, corrections had to be made for perspective effects, for the non-alignment of the centrelines of the pipe and the camera, and for the reflection of light by stainless steel particles.

The perspective correction is illustrated in figure 3 and described in the thesis by Young (1989). It arises because the particle is at different axial locations when the sequential illuminations are carried out. Particles can thus indicate apparent outward radial movement even when they are moving only in the axial direction. To correct for perspective, an axial particle position and velocity are needed for each image. When five images of a particle were produced, the particle was assumed to be located exactly at the centre of the 5 cm high measurement volume when the third image was produced. For three and four particle images, similar assumptions were made. The axial particle velocity needed to calculate the axial positions of the other images in the group was calculated based on an assumed turbulent velocity profile for pipe flow and the calculated free-fall particle velocity in a stagnant medium. Figure 3 shows how both assumptions are used.

Even though great care was taken, the alignment of the centrelines of the pipe and camera was never exact. Because of perspective effects, the image of the pipe wall had a finite thickness. For perfect alignment, this thickness is uniform around the pipe circumference. For slight misalignment, the thickness is skewed. For the multiple image technique, the pipe-wall image used for particle image reference was always the one at the top of the measurement volume. The alignment correction is thus zero for particles located at the top of the measurement volume and increases proportionately with axial distance away from the top. At the bottom of the volume, the correction is half of the difference between the widest and narrowest parts of the image of the pipe wall. The correction is applied only in the direction of the diameters connecting the widest and narrowest parts of the wall image thickness.

For the multiple image measurements, each particle image was produced from only one flash unit. Since the stainless steel particles gave off light mainly by surface reflection, the light rays from the illuminated particles that are reflected to the camera lens do not originate at the centre of the particle. The net effect of this is that the images show an added zigzag motion because consecutive flashes originated on opposite sides of the pipe. The correction for this was to move each image position by a fixed amount.

Once the appropriate corrections were applied, a particle trajectory could be calculated for each group of particle positions produced by a single particle. For convenience, the particle positions were converted from Cartesian to cylindrical polar coordinates. This gave $r_i$ and $\theta_i$ where $i$ is the $i$th particle position. Interpolating polynomial schemes were then used to convert the $r_i$ and $\theta_i$ positions into $r(t)$ and $\theta(t)$. For three particle images, two quadratics in time were used to define the path. For four images, two cubics in time were used. For five images, two cubic splines were used.

For averaging purposes, the cross-section of the pipe was divided into forty-nine concentric rings with a centre circle. Velocities, $V_r = \mathrm{d}r/\mathrm{d}t$ and $V_\theta = r(\mathrm{d}\theta/\mathrm{d}t)$, and rates of change of velocity, $A_r = \mathrm{d}V_r/\mathrm{d}t$ and $A_\theta = \mathrm{d}V_\theta/\mathrm{d}t$, were calculated at several fixed and evenly spaced time intervals along each particle path. This facilitated the treatment of trajectories that crossed between concentric rings while being photographed and weighted the particle trajectories according to the total time that they were monitored. For three, four, and five measured particle positions, calculations were, respectively, made at 10, 15, and 20 positions when the delay timers were set at one delay setting. For different delay timer settings, the weightings change in proportion to the ratio of the new delay time to the old one.

## 4. Results

### 4.1. *Lagrangian diffusion coefficients*

Particle number concentration profiles were calculated from single flash experiments by counting the number of particles in concentric radial rings and dividing by the area of the ring. Figures 4 (*a*) and 4 (*b*) present typical concentration profiles obtained

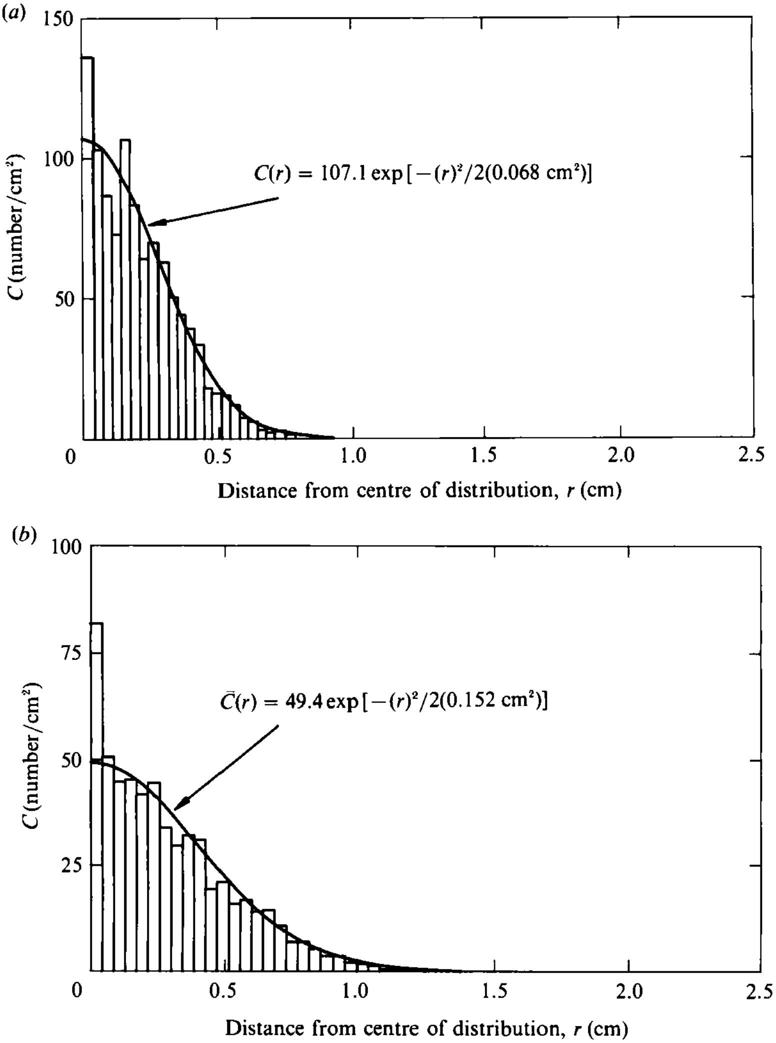

FIGURE 4. (*a*) Particle number concentration profile for glass spheres at $z = 10$ cm, run 5. (*b*) Particle number concentration profile for glass spheres at $z = 17.5$ cm, run 5.

by analysing several photographs. These figures are for glass spheres that were injected into water that was flowing down the pipe at a Reynolds number of 140000. The measurements in figure 4(*a*) were made at a distance of $z = 10$ cm from the injector at a friction velocity of $v^* = 12.07$ cm/s and a centreline velocity of $U_c = 316$ cm/s. They were obtained from 1016 particle images. The measurements in figure 4(*b*) were made at a distance of 17.5 cm for $v^* = 12.33$ cm/s and $U_c = 323$ cm/s. They were obtained from 1382 particle images. The concentrations at small $r$ were subject to large statistical errors because of the small areas they sampled. Each of the profiles was fitted with a Gaussian distribution function to calculate values of $\overline{X_p^2} = 0.068$ cm² and 0.152 sm².

Figure 5 shows measurements of $\overline{X_p^2}$ versus time for concentration profiles that were obtained at distances of 10, 15, 20, 25 and 52.5 cm from the injector tip. The time, $t$, was calculated from

$$t = z/(U_c + V_T), \tag{19}$$

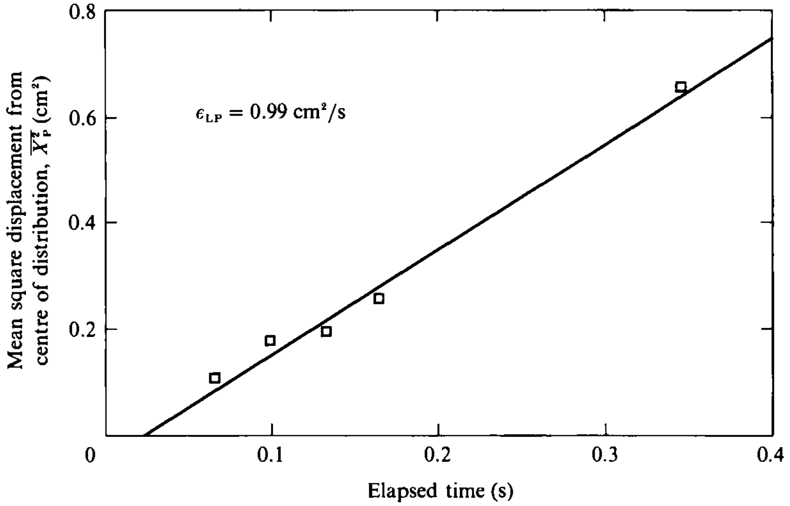

FIGURE 5. Dispersion as a function of time, run 8.

| Run | $U_c$ (cm/s) | $v^*$ (cm/s) | $z$ (cm) | $\dot{V}_{inj}$ (cm³/s) | $\epsilon_{LP}$ (cm²/s) | $N$ (points) | $\epsilon_{LP}/v^*R$ |
|---|---|---|---|---|---|---|---|
| 5 | 320 | 12.2 | 10–25 | 0.79 | 1.99 | 1016–1621 | 0.064 |
| 6 | 211 | 8.36 | 10–25 | 0.49 | 1.81 | 1388–1013 | 0.085 |
| 7 | 211 | 8.36 | 10–25 | 0.61 | 1.83 | 993–1316 | 0.086 |
| 8 | 151 | 6.16 | 10–52.5 | 0.33 | 0.99 | 1082–794 | 0.063 |
|  |  |  |  |  |  |  | 0.074 = av. |

TABLE 1. Results for $\epsilon_{LP}$ of glass spheres

where $U_c$ is the centreline fluid velocity and $V_T$ is the terminal velocity. A turbulent Lagrangian diffusion coefficient, defined by (3), can be calculated from the slope of a straight line through these data. Values of $\epsilon_{LP}$ obtained in this way are summarized in table 1. It should be noted that the two runs for $U_c = 211$ cm/s with different injection velocities gave the same $\epsilon_{LP}$.

### 3.2. *Turbulent velocities*

For measurements of multiple positions of particles, the 5 cm high illuminated region was positioned between 389 and 394 cm downstream of the injection tip. The conditions for the runs are listed in table 2. It should be noted that the particles were not generally injected at the centreline velocity in these experiments. Parameters characterizing these runs are given in table 3. Here $V_T$ is the terminal free-fall velocity and $Re_T$ is a particle Reynolds number based on this velocity. Parameter $\tilde{\beta}$ is the reciprocal of the inertial time constant of the particle, defined by (11). The Lagrangian timescale of the fluid, $T_{LF}$, was calculated from a correlation of measurements presented by Vames & Hanratty (1988). Term $\tilde{\beta}T_{LF}$ was a large number for all of the runs, which indicates that particle inertia effects do not cause

| Run | Material | $T$ (°C) | $\dot{V}_{\text{inj}}$ (cm$^3$/s) | $Re$ | $v^*$ (cm/s) |
|---|---|---|---|---|---|
| 1 | glass | 24.2 | 0.33 | 70800 | 6.30 |
| 2 | glass | 24.6 | 0.33 | 16400 | 1.72 |
| 3 | s.s. | 25.5 | 0.33 | 72900 | 6.28 |
| 4 | s.s. | 22.7 | 0.33 | 15700 | 1.73 |

TABLE 2. Conditions for the velocity measurements

| Run | Material | $\tilde{\beta}$(s$^{-1}$) | $V_{\text{T}}$ (cm/s) | $Re_{\text{T}}$ | $\tilde{\beta}T_{\text{LF}}$ | $V_{\text{T}}^+$ | $\tau^+$ |
|---|---|---|---|---|---|---|---|
| 1 | glass | 608 | 0.79 | 0.86 | 33.8 | 0.12 | 7.1 |
| 2 | glass | 604 | 0.79 | 0.88 | 123.0 | 0.46 | 0.54 |
| 3 | s.s. | 253 | 3.19 | 3.60 | 14.1 | 0.51 | 17.6 |
| 4 | s.s. | 265 | 3.05 | 3.23 | 53.8 | 1.77 | 1.2 |

TABLE 3. Parameterization of the data

a lag from the turbulent fluid motions. The ratio of the free-fall velocity to the friction velocity, designated by $V_{\text{T}}^+$, was high enough that the crossing of trajectories could have an effect in runs 2, 3, and 4. Parameter

$$\tau^+ = \frac{v^{*2}}{\tilde{\beta}\nu} \tag{20}$$

is listed in the last column in table 3. Runs 1, 2, and 4 have values of $\tau^+$ characteristic of aerosol particles in air; that is, the stopping distances are small compared to the thickness of the viscous wall layer.

Measurements of the root-mean-square of the radial components of particle velocity fluctuations, $(\overline{v_{\text{R}}^2})^{\frac{1}{2}}/v^*$, for glass spheres at $Re = 70800$ and for stainless steel spheres at $Re = 72900$ are compared with Laufer's (1954) measurements with a hot-wire anemometer in figure 6. It is to be noted that the same results are obtained with stainless steel and with glass spheres. The good agreement with the measurements of Laufer indicates that the particles were rapidly responding to the turbulent velocity fluctuations and that the optical methods described in this paper give reliable results. The measurements of $(\overline{v_\theta^2})^{\frac{1}{2}}/v^*$, shown in figure 6, again show good agreement between the results with glass and stainless steel particles. The slight disagreement with the measurements of Laufer could reflect small errors in the hot-wire measurements.

Measurements of $(\overline{v_{\text{R}}^2})^{\frac{1}{2}}/v^*$, $(\overline{v_\theta^2})^{\frac{1}{2}}/v^*$ at a low Reynolds number (runs 2 and 4) are shown in figure 7. Again the experiments with glass spheres and stainless steel spheres give the same result. This is of interest since the stainless steel particles had a large free-fall velocity, and indicates that particles will follow the fluid velocity fluctuations for large $\tilde{\beta}T_{\text{LF}}$, even if 'the crossing of fluid trajectories' (large $V_{\text{T}}^+$) is important. Because the experiment in figure 7 are at low Reynolds numbers, the viscous wall region occupies a large portion of the pipe radius (0.1 $R$). One can expect agreement between experiments at different Reynolds numbers in a plot that uses the pipe radius, $R$, to normalize wall distances only for $y^+ > 40$. The good agreement of the measurements of $\overline{v_{\text{R}}^2}$ and $\overline{v_\theta^2}$ for $y^+ > 40$ at the two different Reynolds adds further confidence in the accuracy of the optical method and in the interpretation that the magnitudes of the particle and fluid velocity fluctuations are the same.

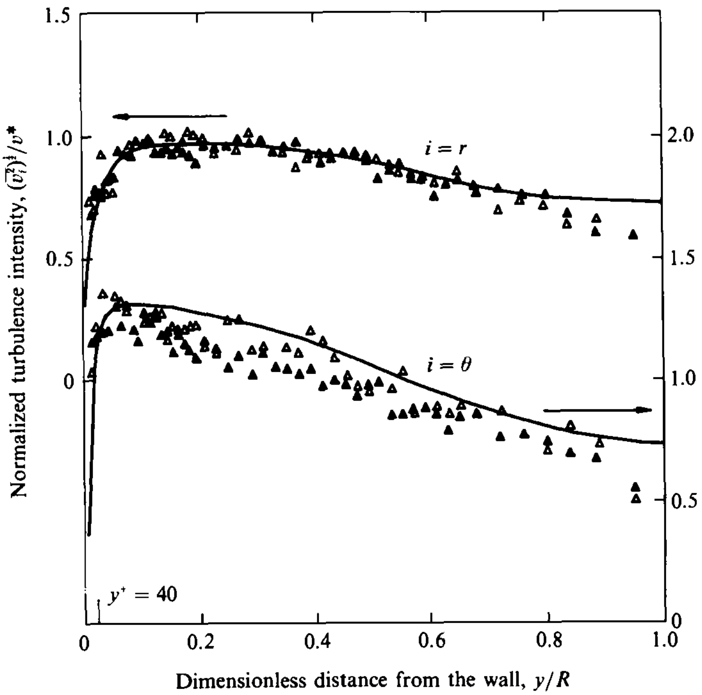

FIGURE 6. Radial and azimuthal turbulent intensities of the particles for $Re = 70800$ and $72900$. △, glass; $\beta\tau_{FL} = 33.8$; $V_T^+ = 0.12$, $\tau^+ = 7.1$. ▲, stainless steel; $\beta\tau_{FL} = 14.1$, $V_T^+ = 0.51$, $\tau^+ = 17.6$. —, Laufer (1954), $Re = 41000$.

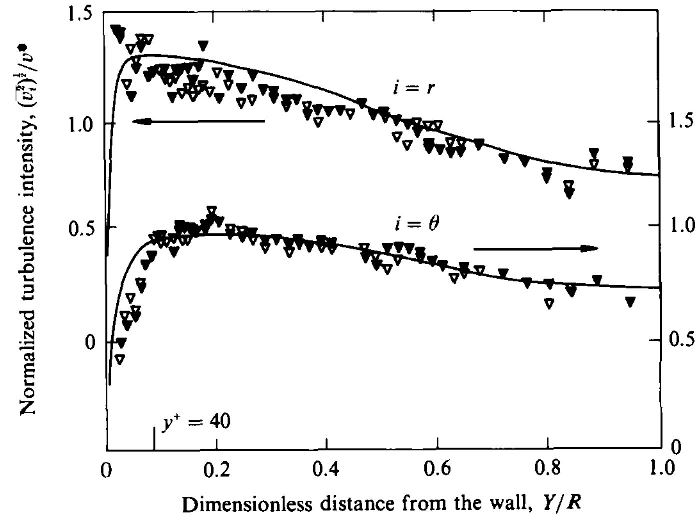

FIGURE 7. Radial and azimuthal turbulent intensities of the particles for $Re = 16400$ and $15700$. ▽, glass; $\beta\tau_{FL} = 123$, $V_T^+ = 0.46$, $\tau^+ = 0.54$. ▼, stainless steel; $\beta\tau_{FL} = 53.8$, $V_T^+ = 1.77$, $\tau^+ = 1.2$. —, Laufer (1954), $Re = 41000$.

### 3.3. *Eulerian diffusion coefficients*

Eulerian diffusion coefficients were evaluated in two experiments. One of these was done with glass spheres. It was carried out between 49 and 54 cm downstream from the injector and was performed under the same conditions as the run at $U_c =$

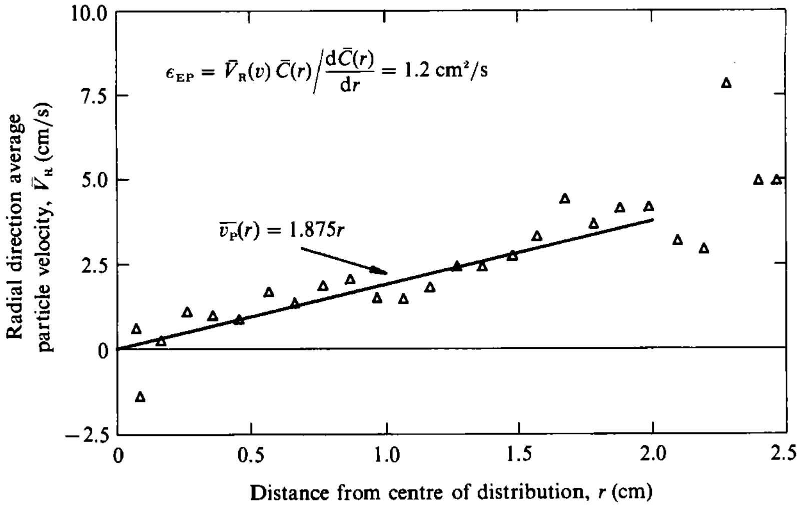

FIGURE 8. Average particle velocity in the radial direction, run 9.

151 cm/s listed in table 1. Measurements of $\bar{V}_\theta$ obtained from multiple image experiments gave a value of zero. Measurements of $\bar{V}_R$, shown in figure 8, are fitted reasonably well by the linear relation

$$\bar{V}_R = kr, \tag{21}$$

where $k = 1.875\ \mathrm{s^{-1}}$.

Since $N(r) = \overline{V_R C}$, equation (2) gives

$$\epsilon_{EP} = \bar{V}_R\,\bar{C}\Big/\left(-\frac{d\bar{C}}{dr}\right). \tag{22}$$

Measurements presented earlier show that $\bar{C}$ can be fitted with a Gaussian distribution for which

$$\bar{C}\Big/\frac{d\bar{C}}{dr} = -\frac{\overline{X_P^2}}{r}. \tag{23}$$

From (22) and (23)

$$\epsilon_{EP} = k\overline{X^2}. \tag{24}$$

Therefore, within the accuracy of the experiments, the Eulerian diffusion coefficients, at a given $z$, can be represented by a constant value independent of $r$ outside the viscous wall region.

The results from the single image experiments, shown in figure 5, give $\overline{X_P^2} = 0.65\ \mathrm{cm^2}$ at $z = 52.5$ cm. The mean-squared displacement could also be calculated from a concentration profile obtained by considering the particle images formed by only the third light sheet in the multiple image experiments. The concentration profile obtained in this way gives a value of $\overline{X_P^2} = 0.64\ \mathrm{cm^2}$ at $z = 51.5$ cm, in good agreement with the result from the single image experiments.

For this experiment a value of $\epsilon_P = 1.2\ \mathrm{cm^2/s}$ was calculated using $\overline{X_P^2} = 0.64\ \mathrm{cm^2}$. In comparison, table 1 gives a value of $\epsilon_{LP} = 0.99\ \mathrm{cm^2/s}$ for experiments under the same conditions. A 20% difference exists between the measured values of $\epsilon_{EP}$ and $\epsilon_{LP}$. This is probably due to errors associated with establishing the limiting slope of the $\overline{X_P^2}$ versus time curve from the small amount of data shown in figure 5.

It appears that the direct measurement of $\bar{V}_R$ is a better way to establish long-time diffusion coefficients than are measurements of dispersion from a point source. A value of $\epsilon_{EP}/v^*R = 0.077$ is obtained from the multiple flash experiment. It is noted from Table 1 that this is in good agreement with the average value of

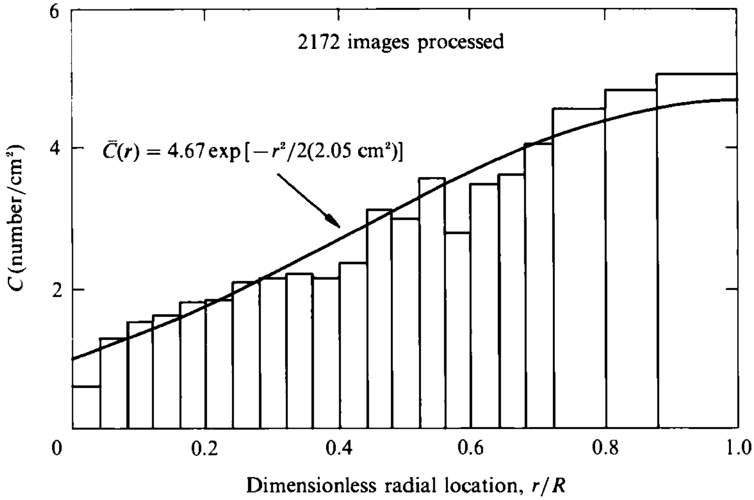

FIGURE 9. Number concentrations of particles for run 4.

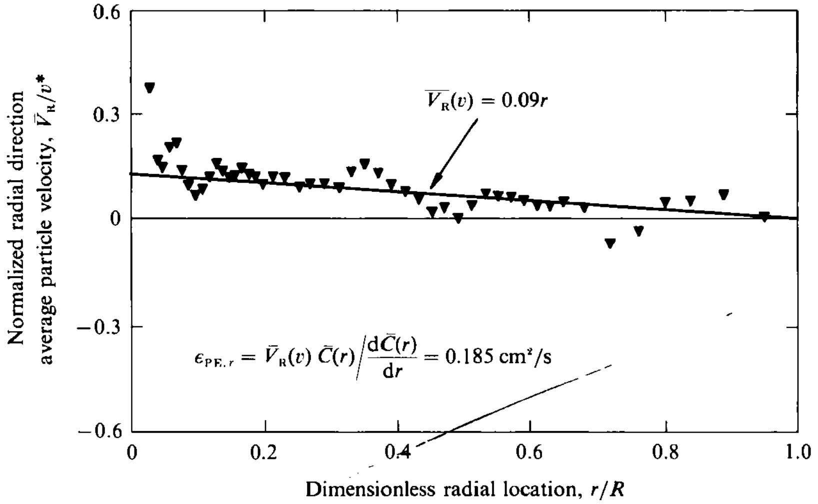

FIGURE 10. Average particle velocities in the radial direction, run 4.

$\epsilon_{LP}/v^*R = 0.074$ obtained from the four runs that used dispersion measurements. It is also in agreement with the value of $\epsilon_{EP}/v^*R = 0.074$ given for diffusion of fluid particles (Vames & Hanratty 1988).

The second experiment in which Eulerian diffusion coefficients were measured used stainless steel spheres. The experimental conditions were the same as for run 4 listed in table 2. The concentration profile is given in figure 9. For this experiment particles were trapped in the slow moving fluid close to the wall so there is a net transfer of particles to the wall. Regardless, the concentration profile could still be fitted with a Gaussian curve. Measurements of $\bar{V}_R/v^*$ are shown in figure 10. These are roughly fitted with a linear relation. From (22) and the results in figures 9 and 10, a value of $\epsilon_{EP} = 0.185\ \mathrm{cm}^2/\mathrm{s}$ is obtained.

For the conditions of the run this gives $\epsilon_{EP}/v^*R = 0.042$. It is to be noted that this is much lower than the value of $\epsilon_{LF}/v^*R = 0.074$ given by Vames & Hanratty. In fact $\epsilon_{EP}/\epsilon_{LF}$ is found to be 0.57. These results show, for large $\tilde{\beta}T_{LF}$, that the 'crossing of trajectories', associated with large $V_T^+$, can cause a decrease in the turbulent diffusion

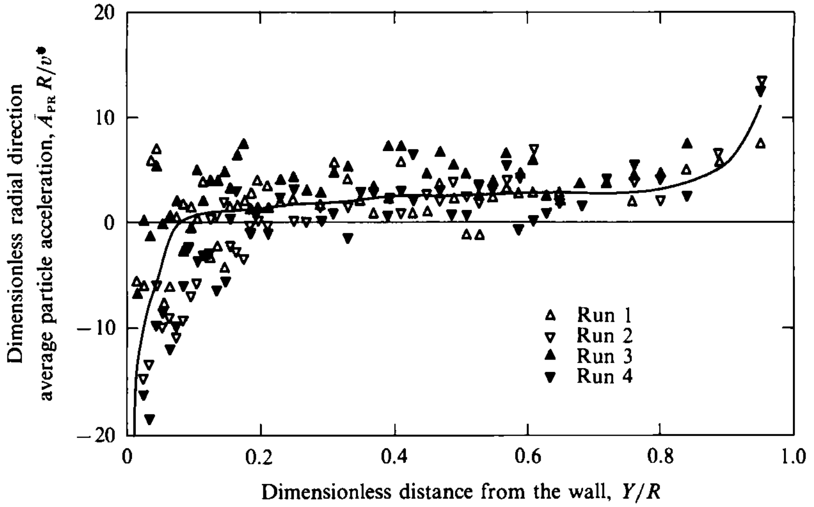

FIGURE 11. Rate of change of $\bar{V}_R$ for all of the runs listed in table 2. The solid curve is calculated with (29).

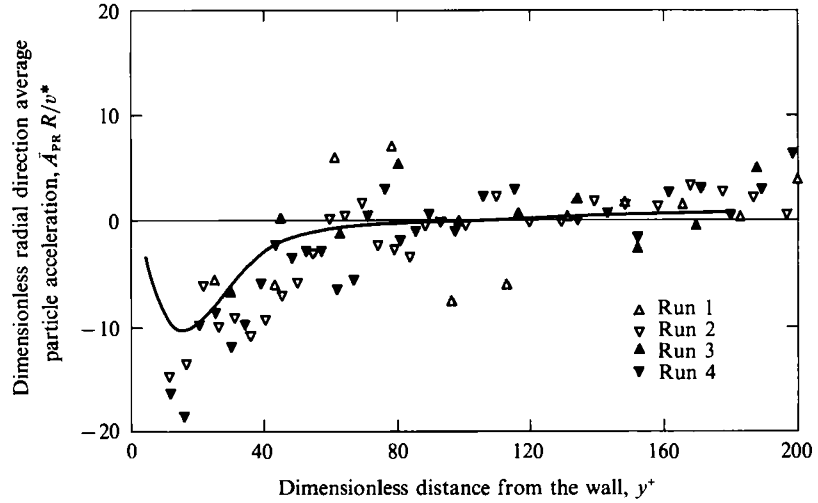

FIGURE 12. The rate of change of $\bar{V}_R$ near the wall. The solid curve is calculated with (29).

coefficient without affecting the magnitude of the turbulent velocity fluctuations of the particles.

### 3.4. *Rate of change of particle velocity*

The measurements of the rate of change of the velocity in the radial direction, $\bar{A}_{PR}$, for all of the runs listed in table 2 are plotted in figure 11. Here the acceleration is made dimensionless with $v^*$ and $R$ and the distance from the wall, $y$, is made dimensionless with $R$. Measurements for stainless steel and glass spheres agree when compared at the same flow rate. The interesting feature of these results is that the sign of $\bar{A}_R$ changes. For the low flow rate this occurs at $y/R \approx 0.2$ and for the high flow rate, at $y/R \approx 0.05$. This can be understood better when the measurements are plotted against $y$ made dimensionless with wall parameters, as shown in figure 12. Here it is seen that the change in sign occurs in the range $y^+ = 80$–$120$. This corresponds to the location of a maximum in the root-mean-square of the radial

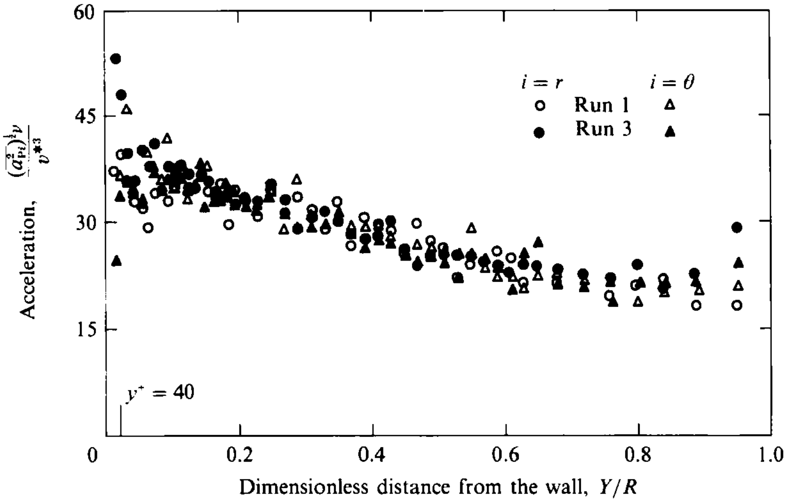

FIGURE 13. Root-mean-square of the fluctuations in the rate of change of $V_i$ for runs 1 and 3.

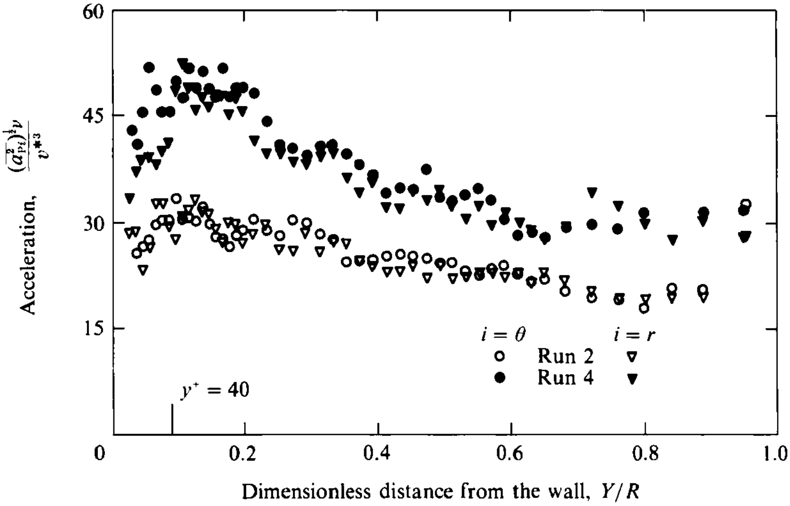

FIGURE 14. Root-mean-square of the fluctuations in the rate of change of $V_i$ for runs 2 and 4.

velocity fluctuations. The averages of $A_\theta$ showed no trend and were approximately zero.

The behaviour in figure 11, appears to be related to the spatial variation of $\overline{v_R^2}$ or of $\overline{u_R^2}$. For $y^+ > 80$–120, movements in the $+r$ direction (or $+V_R$) are from regions of low $\overline{u_R^2}$ to high $\overline{u_R^2}$ and are likely to be associated with an increase in the positive value of $V_R$ (a positive rate of change). Also, movements in the $-r$ direction (or $-V_R$) are from regions of high $\overline{u_R^2}$ to low $\overline{u_R^2}$ so they are likely to be associated with a decrease in the negative value of $V_R$ (a positive rate of change). Similar type arguments can be used to rationalize the measured negative accelerations for $y^+ < 80$–120.

Fluctuations in the time rate of change in velocity, $a_i$, were calculated by subtracting $\overline{A_i}$ from $A_i$. Measurements of the root-mean-square radial, $(\overline{a_{PR}^2})^{\frac{1}{2}}$, and azimuthal, $(\overline{a_{P\theta}^2})^{\frac{1}{2}}$, fluctuations are normalized with the friction velocity and pipe radius and plotted against the distance from the wall made dimensionless with the pipe radius in figures 13 and 14. Results for the high Reynolds number runs listed in table 2 (runs 1 and 3) are presented in figure 13. It is noted that there is good agreement between the results with stainless steel and glass spheres, and that $\overline{a_{PR}^2} = \overline{a_{P\theta}^2}$. Results for runs 2 and 4 are presented in figure 14. The root-mean-square values of the fluctuations in the $\theta$- and $r$-directions are again found to be approximately equal. The most interesting feature in figure 14 is that fluctuations of $A_t$ are larger for the stainless steel spheres. Because of the effect of crossing of trajectories, these particles experience much stronger increases and decreases in velocity than the glass spheres, at the low flow, even though the profiles of $\overline{A}_R$ and $\overline{v_R^2}$ are the same. The multiple image photographs clearly showed this difference in that a substantial portion of the trajectories of the stainless steel spheres show sudden changes in direction. These sudden changes indicate that high instantaneous accelerations and decelerations occur when the particle falls from one region of highly correlated flow to another.

Some understanding of the measurements in figures 11–14 can be obtained by recognizing that the rate of change of particle velocity is given by

$$A_t = \frac{\partial V_t}{\partial t} + V_R\frac{\partial V_t}{\partial r} + \frac{V_\theta}{r}\frac{\partial V_t}{\partial \theta} + V_z\frac{\partial V_t}{\partial z}. \tag{25}$$

Now, if changes of the particle concentration are ignored conservation of mass dictates that

$$0 = V_R\left(\frac{\partial V_R}{\partial r} + \frac{V_R}{r} + \frac{1}{r}\frac{\partial V_\theta}{\partial \theta} + \frac{\partial V_z}{\partial z}\right). \tag{26}$$

From (25) and (26)

$$\overline{A}_R = \frac{1}{r}\frac{\partial\overline{(rV_R^2)}}{\partial r} + \frac{1}{r}\frac{\partial\overline{(V_R V_\theta)}}{\partial \theta} + \frac{\partial}{\partial z}\overline{V_R V_Z}). \tag{27}$$

Because of symmetry and because the particle field is fully developed

$$\overline{A}_R = \frac{1}{r}\frac{\mathrm{d}(r\overline{V}_R^2)}{\mathrm{d}r} + \frac{1}{r}\frac{\mathrm{d}\,\overline{(rv_R^2)}}{\mathrm{d}r}. \tag{28}$$

Now, if the system is approximately in equilibrium so that $\overline{V}_R^2 \ll \overline{v_R^2}$, (28) is simplified to

$$\overline{A}_R = \frac{1}{r}\frac{\partial}{\partial r}(r\,\overline{v_R^2}). \tag{29}$$

The solid curves shown in figures 11 and 12 were calculated from (29) by assuming $\overline{v_R^2} = \overline{u_R^2}$ and by using Laufer's measurements of $\overline{u_R^2}$ at $Re = 41000$ for $y^+ > 40$ and a supercomputer simulation of turbulent channel flow (Lyons 1989) for $y^+ < 40$. Reasonably good agreement with the measurements is indicated.

The $r$-component of the equation of particle motion can be written as

$$A_R - \frac{v_\theta^2}{r} = \tilde{\beta}(U_R - V_R). \tag{30}$$

Since $\overline{U}_R = 0$, the time-average of (30) gives the following if (29) is substituted for $\overline{A}_R$:

$$\overline{V}_R = -\frac{1}{\beta}\left(\frac{\partial\overline{v_R^2}}{\partial r} + \frac{\overline{v_R^2}}{r} - \frac{\overline{v_\theta^2}}{r}\right). \tag{31}$$

This is the turbophoretic velocity expressed in cylindrical polar coordinates so the measurements of $\overline{A}_R$ are related to this concept. [The authors are indebted to one of the reviewers for his pointing out this simple interpretation of turbophoresis.]

Again, the following relation is obtained for $a_i = A_i - \bar{A}_i$ from the equation of motion:

$$\overline{a_i^2} = \tilde{\beta}^2 \overline{(u_i - v_i)^2}. \tag{32}$$

This equation shows that, even though $\overline{u_i^2} = \overline{v_i^2}$, the particles do not follow the fluid velocity fluctuations exactly since $\overline{a_i^2}$ is finite. The measurements of the particle acceleration can be considered as giving $\overline{(u_i - v_i)^2}$. For the case of $\overline{u_i^2} \approx \overline{v_i^2}$ represented by runs 1–4, (32) can be written as follows:

$$\frac{R^2}{v^{*4}}\overline{\left(\frac{\mathrm{d}v_i}{\mathrm{d}t}\right)^2} = 2\left(\frac{\overline{u_i^2}}{v^{*2}}\right)(\tilde{\beta}T_{\mathrm{LF}})^2\left(\frac{T_{\mathrm{LF}}\,v^*}{R}\right)^{-2}\left(1 - \frac{\overline{u_i v_i}}{\overline{u_i^2}}\right). \tag{33}$$

From Vames & Hanratty (1988) the dimensionless $T_{\mathrm{LF}}$ is roughly constant. The results in figures 13 and 14 could reflect the magnitude of the correlation between the particle and fluid motion, $\overline{u_i v_i}$. From (33), the increase in the dimensionless root-mean-square of $a_{pi}$ with increasing $r$ is consistent with the increase of $(\overline{u_i^2}/v^{*2})$. The degree to which the correlation coefficient differs from unity appears to depend on $\tilde{\beta}T_{\mathrm{LF}}$ and $V_{\mathrm{T}}/v^*$. For runs 1, 2, 3, for which the effect of the crossing of trajectories does not appear to be important, (33) suggests that $[1 - (\overline{u_i v_i}/\overline{u_i^2})]$ is inversely proportional to $(\tilde{\beta}T_{\mathrm{LF}})^2$.

## 5. Discussion

### 5.1. *Accuracy of the measurement technique*

The chief limitation in the results obtained was that the manual method for analysing photographs reduced the accuracy of statistical results because, for practical reasons, the number of particle trajectories analysed was not as large as desired. The use of image processing techniques would greatly facilitate the measurements.

An important factor in the accuracy of the results is the selection of a time interval between flashes. It was desirable for the average number of particles in a group to be 3.5–4. Figure 15 shows the effect of the time interval for run 1 in table 2. It is noted that a flash interval of $\Delta t = 0.00667$ s was superior to a $\Delta t = 0.00900$ s. In fact the use of $\Delta t = 0.00667$ s ensured that a proper number of images was obtained from the pipe centre to $y^+ \sim 120$ for this set of conditions. The use of a larger $\Delta t$ captured more desirable samples close to the wall but was not satisfactory in the central regions of the pipe.

Figure 16 gives the number of trajectories (with 3 or more images) that were analysed for all of the runs listed in table 2. This clearly shows the inadequacy of the multiple image technique close to the wall and at the pipe centre. The small number of samples close to the wall resulted because the chosen $\Delta t$ of the flashes was too small to capture enough of the slow moving particles. The $\Delta r$ of the three rings close to the pipe centre is relatively large, but the probability of finding a particle there is smaller than in other parts of the pipe because the cross-sections of the rings are smaller.

### 5.2. *Turbulent velocity fluctuations and turbulent diffusivities*

The results obtained show for large $\tilde{\beta}T_{\mathrm{LF}}$ that the root-mean-square of the turbulent velocity fluctuations of the particles is approximately equal to the root-mean-square of the turbulent velocity fluctuations of the fluid, even for the case of large slip velocities. For large $\tilde{\beta}T_{\mathrm{LF}}$ the turbulent diffusivities of the solid particles were found

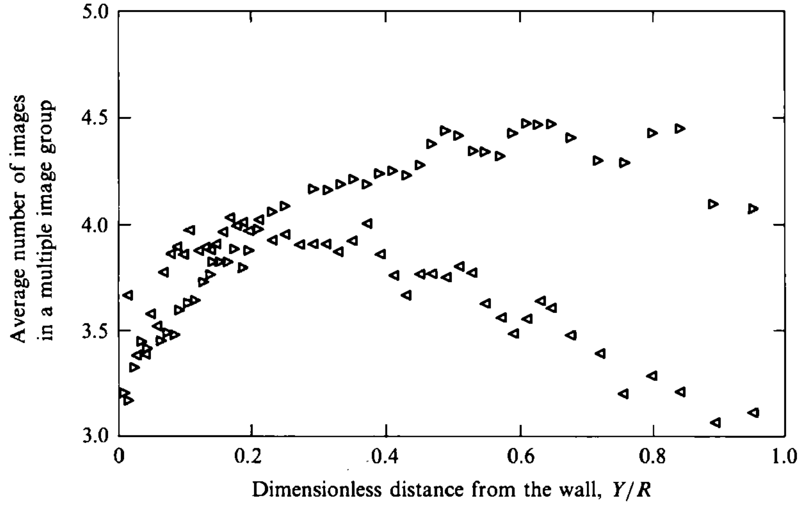

FIGURE 15. Effect of the interval between flashes on the average number of images in a multiple image group for run. 1. ▷, $\Delta t_{\text{flash}} = 0.00667$ s; ◁, $\Delta t_{\text{flash}} = 0.00900$ s.

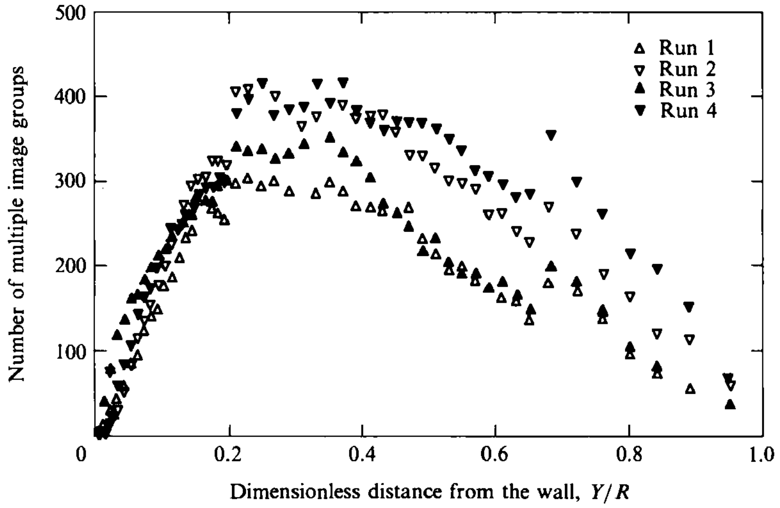

FIGURE 16. Number of multiple image groups analysed as a function of radical position.

to be approximately equal to the turbulent diffusivities of the fluid particles if the slip velocity is not too large. For large slip velocities the diffusivities of the solid particles are less than that of the diffusivities of the fluid particles because of the effect of the crossing of trajectories. This is in agreement with theoretical results obtained by Reeks (1977), Pismen & Nir (1978) and Nir & Pismen (1979) for an isotropic field using a spectral representation of the fluid turbulence which would be strictly valid for low Reynolds numbers.

For example, if the fluid turbulent diffusion coefficient is taken as $\epsilon_{\text{LF}} = 0.074\ v^*R$ the analysis of Reeks predicts that the ratio of particle/fluid mean-squared velocity fluctuations is 0.993 to 1.000 for the range of conditions listed in tables 1 and 2. A comparison of the predicted and measured turbulent diffusion coefficients are summarized in table 4.

| Run | Material | $v^*$ (cm/s) | $V_T^+$ | $\epsilon_{LP}/\epsilon_{LF}$ | | $\epsilon_{EP}/\epsilon_{LF}$ | Reeks<br>$\epsilon_{LP}/\epsilon_{LF}$ |
|---|---|---|---|---|---|---|---|
| 5 | glass | 12.2 | 0.065 | 0.86 | av. = 1.0 | — | 0.99 |
| 6 | glass | 8.4 | 0.095 | 1.14 | | — | 0.99 |
| 7 | glass | 8.4 | 0.095 | 1.16 | | — | 0.99 |
| 8 | glass | 6.2 | 0.13 | 0.85 | | — | 0.99 |
| figure 9 | glass | 6.2 | 0.13 | — | | 1.04 | 0.99 |
| figure 10 | s.s. | 1.73 | 1.77 | — | | 0.57 | 0.62 |

TABLE 4. Comparison of measurements with the analysis of Reeks

### 5.3. *Turbophoresis*

The $\bar{V}_R$ associated with diffusion arises because of concentration gradients so the measured values of $d\bar{V}_R/dt$ presented in figures 11 and 12 cannot be the result of the turbulent diffusion process. This is supported by the observation that the same results are obtained for runs where the solids were uniformly distributed (runs 1, 2, 3) and for runs where concentration gradients existed (run 4).

The agreement of the measurements with (29) lends some indirect support to the analysis that leads to the prediction of turbophoresis effects. A more direct test would be through measurements of $\bar{V}_R$. However, such a comparison would require a consideration of how turbulence non-homogeneities can also cause a time-averaged force on the particle through a time-averaged pressure gradient in the fluid, given as

$$-\frac{\partial \bar{p}}{\partial r} = \rho_F\left[\frac{\partial \overline{u_R^2}}{\partial r} - \frac{\overline{u_\theta^2}}{r} + \frac{\overline{u_r^2}}{r}\right]. \tag{34}$$

The average velocity caused by turbulence non-homogeneities then is

$$\bar{\beta}\,\bar{V}_R = \left(\frac{\partial \overline{v_R^2}}{\partial r} + \frac{\overline{v_R^2}}{r} - \frac{\overline{v_\theta^2}}{r}\right) - \alpha\left(\frac{\partial \overline{u_R^2}}{\partial r} + \frac{\overline{u_r^2}}{r} - \frac{\overline{u_\theta^2}}{r}\right), \tag{35}$$

where $\alpha = 3\rho_F/(2\rho_P+\rho_F)$. It is noted that for $(\rho_P/\rho_F) = 1$ that $\bar{V}_R = 0$ and that as $\rho_P/\rho_F$ increases, the term resulting from fluid pressure gradients becomes less important.

A comparison of measured $\bar{V}_R$ with (35) is not easily accomplished because the drift velocity caused by turbulence non-homogeneities is often small and because other factors, such as turbulent diffusion, and lift forces can contribute to $\bar{V}_R$. A more reliable test would be to measure $\bar{V}_R$ and concentration profiles under fully developed conditions. The net $\bar{V}_R$ should equal zero since the flux caused by concentration gradients would then exactly balance the flux associated with non-homogeneities in the turbulence. The concentration profile would be calculated from (22) using the negative of the value of $\bar{V}_R$ given by (35).

### 5.4. *Lift forces*

Estimates of the possible influences of lift forces is difficult because (16) is strictly valid for laminar flows. One approach has been to use the time-average fluid velocity. If this is done an average of drift velocities due to lift, $\bar{V}_L$, can be calculated from (16) by using the Stokes drag law:

$$\bar{F}_L = 3\pi\mu(d_P)\,\bar{V}_L. \tag{36}$$

For the data shown in figure 8 the calculated velocities due to lift, $\bar{V}_L$, are only about

| Run | $v^*$ (cm/s) | $[\overline{(a_\mathrm{R}^2)}]^{\frac{1}{2}} \approx [\overline{(a_\theta^2)}]^{\frac{1}{2}}$ (cm/s$^2$) | $[\overline{(u_\mathrm{R}-v_\mathrm{R})^2}]^{\frac{1}{2}} \approx [\overline{(u_\theta-v_\theta)^2}]^{\frac{1}{2}}$ cm/s) |
|---|---|---|---|
| 1 | 6.30 | 485 | 0.80 |
| 2 | 6.28 | 485 | 1.92 |
| 3 | 1.72 | 32 | 0.053 |
| 4 | 1.73 | 45 | 0.170 |

TABLE 5. Root mean square accelerations averaged over the pipe cross-section

3% of the measured time-averaged radial velocities. In other cases, however, this type of calculation yields unrealistically high values of $\bar{V}_\mathrm{L}$. For example, for the experiment used to measure a diffusion coefficient for the stainless steel particles, positive lift velocities are calculated which are 30–40% greater than the measured average velocities given in figure 11. If such a correction were applied a negative diffusion coefficient would be calculated. In other cases in which a uniform concentration of particles existed over the pipe cross-section, a zero value of the average radial velocity was measured in contradiction to the prediction of (16) and (36) using the time-averaged velocity gradient.

The conclusion reached is that for $y^+ > 70$ lift forces can be neglected in a turbulent flow and that $\bar{V}_\mathrm{L}$ cannot be estimated using (16), (36) with the time-averaged velocity gradient. A likely explanation is that (16) is not applicable since parameter $\epsilon$, defined by (17), is a small number, except for a region close to the wall. This conclusion is supported by a recent analysis (McLaughlin 1991) which shows that the lift force drops to a value that is 5% of the value of $F_\mathrm{L}$ given by (16) when $\epsilon$ is 0.3.

### 5.5 *Calculation of a slip velocity*

As is indicated in the discussions related to (13), (14), (15) the average relative velocity is needed when the particle drag is not described by Stokes law. Measures of the particle acceleration provide a means to estimate the $|V_\mathrm{R}|$ and to check the accuracy of relation (15) which assumes $\Sigma\,\overline{(v_i-u_i)^2} = 0$.

From (32) it is seen that the measurements in figures 13 and 14 can be used to calculate $\overline{(u_\mathrm{R}-v_\mathrm{R})^2}$ and $\overline{(u_\theta-v_\theta)^2}$. Table 5 presents measurements of the values of $[\overline{(a_\mathrm{R})^2}]^{\frac{1}{2}}$ and $[\overline{(a_\theta)^2}]^{\frac{1}{2}}$ averaged over the pipe cross-section. When these are divided by the estimated $\beta$ listed in table 3 the average magnitude of the velocity difference is found (see table 5).

If it is assumed that the magnitude of the difference in the turbulent velocities of the particle and fluid in the axial direction is the same as in the $r$- and $\theta$-directions the magnitude of the average effective velocity can be calculated from (14). This can be used in (9) or (11) to estimate new values of $\beta$ and $\tilde{\beta}$. These, in turn, can be used in (32) to estimate a new value of the turbulence contribution to the average relative velocity. The results of such an iterative calculation using data from runs 1, 2, 3, 4 are summarized in table 6.

These calculations show that the value of the relative velocity vector doubles for the runs at high velocities but stays approximately unchanged for the runs at low velocities. These results indicate that particles, which are considered Stokesian from the average terminal velocity, may exhibit non-Stokesian properties in high-Reynolds-number turbulent flows. It is also to be noted that the values of $\tilde{\beta}T_\mathrm{LF}$ and $\tau^+$ listed in table 3 for the high velocity runs (1 and 3) are not correct since they are based on a value of $\tilde{\beta}$ estimated from the particle terminal velocity.

| | $\lvert\bar{V}_R\rvert$ (cm/s) | | $Re_p$ | | $\tilde{\beta}$ (s$^{-1}$) | |
|---|---|---|---|---|---|---|
| Run | Old | New | Old | New | Old | New |
| 1 | 0.79 | 1.79 | 0.86 | 1.95 | 608 | 692 |
| 2 | 0.79 | 0.79 | 0.88 | 0.88 | 604 | 604 |
| 3 | 3.19 | 5.49 | 3.60 | 6.20 | 253 | 282 |
| 4 | 3.23 | 3.22 | 3.23 | 3.43 | 268 | 268 |

TABLE 6. Corrected values of the mean relative velocity

This work was supported by the National Science Foundation under NSF CBT 88-00980 and by the Department of Energy under DEF G02-86ER13556.

## REFERENCES

CAPORALONI, M., TAMPIERI, F., TROMBETTI, F. & VITTORI, O. 1975 Transfer of particles in nonisotropic air turbulence. *J. Atmos. Sci.* **32**, 565–568.

CSANADY, G. T. 1963 Turbulent diffusion of heavy particles in the atmosphere. *J. Atmos. Sci.* **20**, 201–208.

GOUESBET, G., DESJONQUERES, P. & BERLEMONT, A. 1988 Eulerian and Lagrangian approaches to turbulent dispersion of particles in transient phenomena in multiphase flow (ed. N. H. Afgan). Hemisphere.

HINZE, J. O. 1975 *Turbulence*, 2nd edn. McGraw Hill.

LAUFER, J. 1954 The structure of turbulence in fully-developed pipe flow. *NACA Rep.* no. 1174.

LEE, M. M., HANRATTY, T. J. & ADRIAN, R. J. 1989 An axial viewing photographic technique to study turbulence characteristics of particles. *Intl J. Multiphase Flow* **15**, 787–802.

LYONS, S. L. 1989 A direct numerical simulation of fully developed turbulence channel flow with passive heat transfer. PhD thesis, University of Illinois, Urbana.

MCCOY, D. D. & HANRATTY, T. J. 1977 Rate of deposition of droplets in annular two-phase flow. *Intl J. Multiphase Flow* **3**, 319.

MCLAUGHLIN, J. B. 1991 Inertial migration of a small sphere in linear shear flows. *J. Fluid Mech.* **224**, 261–274.

MAXEY, M. R. & RILEY, J. J. 1983 Equation of motion for a small rigid sphere in a nonuniform flow. *Phys. Fluids* **26**, 883–889.

NIR, A. & PISMEN, L. M. 1979 The effect of steady drift on the dispersion of a particle in a turbulent field. *J. Fluid Mech.* **94**, 369.

PISMEN, L. M. & NIR, A. 1978 On the motion of suspended particles in stationary homogeneous turbulence. *J. Fluid Mech.* **84**, 193.

REEKS, M. W. 1977 On the dispersion of small particles suspended in an isotropic turbulent fluid, *J. Fluid Mech.* **83**, 529.

REEKS, M. W. 1983 The transport of discrete particles in inhomogeneous turbulence. *J. Aerosol Science* **14**, 729–739.

RISK, M. A. & ELGHOBASHI, S. E. 1985 On the motion of a spherical particle suspended in a turbulent flow near a plane wall. *Phys. Fluids* **28**, 806–817.

SAFFMAN, P. G. 1965 The lift on a small sphere in a slow shear flow. *J. Fluid Mech.* **22**, 385.

SAFFMAN, P. G. 1968 Corrigendum to 'The lift on a small sphere in a slow shear flow'. *J. Fluid Mech.* **31**, 624.

TAYLOR, G. I. 1921 Diffusion by continuous movements. *Proc. Lond. Math. Soc.* **151**, 196.

VAMES, J. S. & HANRATTY, T. J. 1988 Turbulent dispersion of droplets for air flow in a pipe. *Exps Fluids* **6**, 94–104.

YOUNG, J. B. 1989 An experimental study of solid particle motion in a turbulent liquid pipe flow. PhD thesis, University of Illinois, Urbana.

YUDINE, M. I. 1959 Physical considerations on heavy particle diffusion. *Atmospheric Diffusion and Air Pollution Adv. Geophys.* **6**, 185.